Nanoscale

PAPER

View Article Online
View Journal | View Issue

Cite this: *Nanoscale*, 2017, **9**, 15895

3D self-assembly of ultrafine molybdenum carbide confined in N-doped carbon nanosheets for efficient hydrogen production†

Haiqing Wang, Xiaobin Xu, Bing Ni, Haoyi Li, Wei Bian and Xun Wang *

Received 27th July 2017,
Accepted 11th September 2017

DOI: 10.1039/c7nr05500e

rsc.li/nanoscale

Electrochemical water splitting has been intensively pursued as a promising approach to produce clean and sustainable hydrogen fuel. However, the lack of low-cost and high-performance electrocatalysts for the hydrogen evolution reaction (HER) hinders the large-scale application. Herein, we have rationally designed and synthesized 3D self-assembly architectures assembled from ultrafine MoC nanoparticles (0D) uniformly embedded within N-doped carbon nanosheets (2D) for the HER *via* a simple protocol. The well-organized 3D nanostructures are composed of very small MoC nanocrystallites (<2 nm) and free-stretching conductive carbon nanosheets with high specific surface areas and abundant mesopores, which can expose more active sites and facilitate electron/ion transport pathways. Based on the merits of the composition and configuration, the resultant hierarchical 3D self-assembly architectures exhibit remarkable electrocatalytic performance and stability for the HER.

Introduction

Hydrogen is one of the most promising energy source alternatives to fossil fuels to address the global issues of severe global energy shortage and environmental deterioration because of its clean and sustainable features.[1] Electrochemical water splitting to produce hydrogen is the most economical and sustainable method for large-scale hydrogen production, which has been intensively pursued.[2–8] To date, platinum (Pt) or Pt-based materials are the most active catalysts for the hydrogen-evolution reaction (HER), but the low abundance and high cost of Pt severely limited their widespread utilization.[9] Thus, it is urgently needed to develop low-cost and earth-abundant non-noble-metal catalysts replacing Pt for practical applications.

Molybdenum carbide (MoC) materials have aroused great interest as a new class of electrocatalysts for the hydrogen-evolution reaction (HER) owing to their low cost, high chemical stability, and high similarity to platinum-based catalysts.[2,6,10–12] To further enhance the HER activity, it is of great significance to improve the exposure surface of active sites by constructing molybdenum carbide with reduced sizes and unique architectures.[2,13,14] Moreover, due to the poor conductivity of molybdenum carbide, conductive carbon supports, such as graphene nanosheets,[6,15,16] carbon rods,[12] carbon nanotubes[3,17] and MOF-derived carbon particles,[18,19] are generally desired to facilitate the charge transfer between the active sites due to their excellent electron transport properties and chemical stability. Among these conductive supports, two-dimensional (2D) graphene-like nanosheets can provide a higher exposure area of active sites and contact area for the electrolyte and electrocatalyst, which have been considered as an effective substrate.[6,20,21] However, the carbonization of Mo-based-compounds at high temperature causes inevitable aggregation and/or excessive growth of MoC for most situations.[12,22–25] In addition, the carbon nanosheets tend to aggregate due to the strong π-stacking and hydrophobic interactions.[26,27] As a result, the number of exposed active sites and the specific surface area of the electrocatalyst are greatly reduced, which is adverse to the HER activity. Recently, the assembly of these carbon nanosheets into a three-dimensional (3D) architecture has been proved to be one of the efficient ways to achieve an improved activity of electrocatalysts,[26,28] which can be expected to not only avoid the aggregation of active nanoparticles and restacking of 2D nanosheets but also combine the advantages of both microstructures and nanostructures. Nonetheless, 3D structures assembled from carbon nanosheets anchored with well-defined active site nanoparticles have rarely been reported.

Herein, we have rationally designed and synthesized 3D self-assembly architectures assembled from ultrafine MoC nanoparticles uniformly embedded within carbon nanosheets for the HER *via* a simple protocol. The well-organized 3D

Key Lab of Organic Optoelectronics and Molecular Engineering, Department of Chemistry, Tsinghua University, Beijing, 100084, China.
E-mail: wangxun@mail.tsinghua.edu.cn

†Electronic supplementary information (ESI) available. See DOI: 10.1039/c7nr05500e

nanostructures are composed of very small MoC nanocrystallites (<2 nm) and free-stretching conductive carbon nanosheets with high specific surface areas and abundant mesopores, which can expose more active sites and facilitate electron/ion transport pathways. Based on the merits of the composition and configuration, the resultant hierarchical 3D assembly exhibits remarkable electrocatalytic performance for the HER typically under alkaline conditions, where very small overpotentials of 128 mV and 170 mV are required to drive current densities of 10 and 20 mA cm^{-2}, respectively. The unique 3D architectures can also efficiently prevent the excessive growth of ultrafine MoC and the aggregation of carbon nanosheets and thus provide good stability during long-term operation.

Results and discussion

Synthesis of 3D self-assembly architectures: MoC-HAs

The unique three-dimensional (3D) architectures of ultrafine molybdenum carbide confined in nitrogen-doped carbon nanosheet hierarchical architectures (denoted as MoC-HAs) as precious-metal-free HER electrocatalysts were prepared *via* a facile synthetic route. The overall synthesis route of MoC-HAs is illustrated in Fig. 1a, where a mixed solution of water and ethanol, ammonium molybdate (AM, $(NH_4)_6Mo_7O_{24}$) and dopamine (DA) were used as the solvent, Mo precursor and C/N source, respectively. When ammonia was injected into the above mixture, carbonaceous nanosheet hierarchical spheres containing Mo atoms (Mo-HAs) are formed through the self-polymerization of DA under basic conditions and self-assembly processes between the positively charged DA and the negatively charged $[Mo_7O_{24}]^{6-}$ *via* electrostatic interactions.[29] We found that without $[Mo_7O_{24}]^{6-}$, the product *i.e.* polydopamine exhibits a spherical morphology with a size of *ca.* 500 nm (Fig. S1†). By contrast, polydopamine nanosheets containing Mo atoms are formed with the addition of $[Mo_7O_{24}]^{6-}$. We suggested that $[Mo_7O_{24}]^{6-}$ can induce the anisotropic growth of polydopamine *via* the electrostatic interaction between the positively charged DA and negatively charged $[Mo_7O_{24}]^{6-}$, thereby leading to the formation of polydopamine nanosheets. In order to control the morphology and size of MoC-HAs, the effects of ammonium molybdate and volume ratios of water (W) to ethanol (E) were investigated using control experiments. We found that the amounts (10, 20 and 40 mg) of ammonium molybdate (samples denoted as AM-10, 20 and 40) showed negligible effects on the MoC-HAs. However, the as-prepared Mo-HAs (Fig. S2†) evolve from disordered free nanosheets (WE-18) to well-defined 3D nanosheet hierarchical spheres (WE-54 and WE-81) and the outer sizes of building nanosheets increased gradually from 100 nm, 300 nm to 1.2 μm with increasing volume ratios of water to ethanol from 1 : 8, 5 : 4 to 8 : 1. Thus, we suggested that the volume ratios of water to ethanol can well manipulate the morphology and size of MoC-HAs. Considering the fact that $(NH_4)_6Mo_7O_{24}$ is insoluble in ethanol but soluble in water, more $[Mo_7O_{24}]^{6-}$ should be dissolved as the proportion of water was increased in the mixed solvent, which can be certified by the gradually decreased content of MoC in the resultant MoC-HAs from 37.1% in WE-18, 35.9% in WE-54/AM-20 to 30.3% in WE-81 (determined by TGA, Fig. S6†). Therefore, the morphology and size controlled 3D architectures of MoC-HAs should be ascribed to the synergy effects of $[Mo_7O_{24}]^{6-}$ that dominate the formation of nanosheets and the spatial constraint of ethanol deriving from the insolubilization feature of $[Mo_7O_{24}]^{6-}$ in ethanol. The resultant MoC-HAs were obtained by a simple annealing treatment of the as-prepared Mo-HAs in N_2 gas. During the annealing process at 900 °C for 4 h, ultrafine MoC nanocrystallites can be well restricted by *in situ* confined carbonization within the conducting carbon nanosheets. The evolution of the colors of the samples from dark red to black can correspond well to the formation of Mo-HAs and MoC-HAs (Fig. 1b–d).

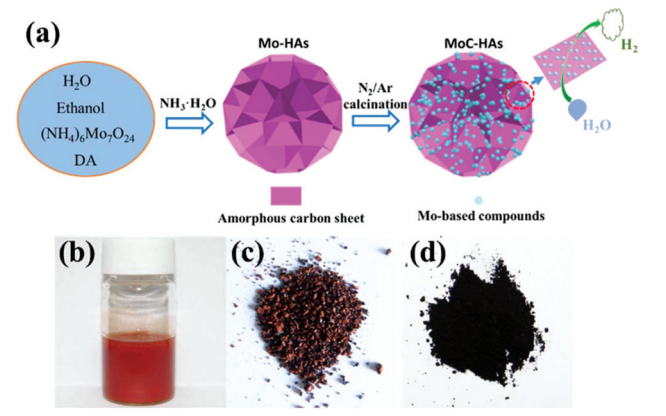

Fig. 1 (a) Schematic representation of the synthesis of MoC-HAs as a nonplatinum HER electrocatalyst. (b, c and d) Digital photographs of a mixture of precursors (b), Mo-HAs (c), and MoC-HAs (d).

Morphology, structure, and composition of Mo-HAs

The morphology, structure and composition of the representative MoC-HAs (AM-20 or WE-54) were systematically studied by using various characterization techniques. The scanning electron microscopy (SEM) of MoC-HAs (Fig. 2a) shows that the product consists of well-defined nanospheres with a homogeneous size-distribution of ~300 nm. A closer observation of high-magnification SEM (Fig. 2b) images indicate that the spheres possess highly rough surfaces and are composed of numerous interconnected nanosheets with a thickness of <5 nm forming the unique three-dimensional (3D) spherical architectures. Transmission electron microscopy (TEM, Fig. 2c) indicates that the MoC nanoparticles are homogeneously anchored throughout the carbon nanosheets of the whole MoC-HAs. The high-angle annular dark-field scanning TEM (HAADF-STEM, Fig. 2d) images of MoC-HAs can further confirm the hierarchical feature of the carbon nanosheets and imply the presence of mesopores arising from interconnected carbon sheets. Local magnified HAADF-STEM images (Fig. 2e and f) can further demonstrate the homogeneous dispersion of MoC nanoparticles throughout the carbon nanosheets of the

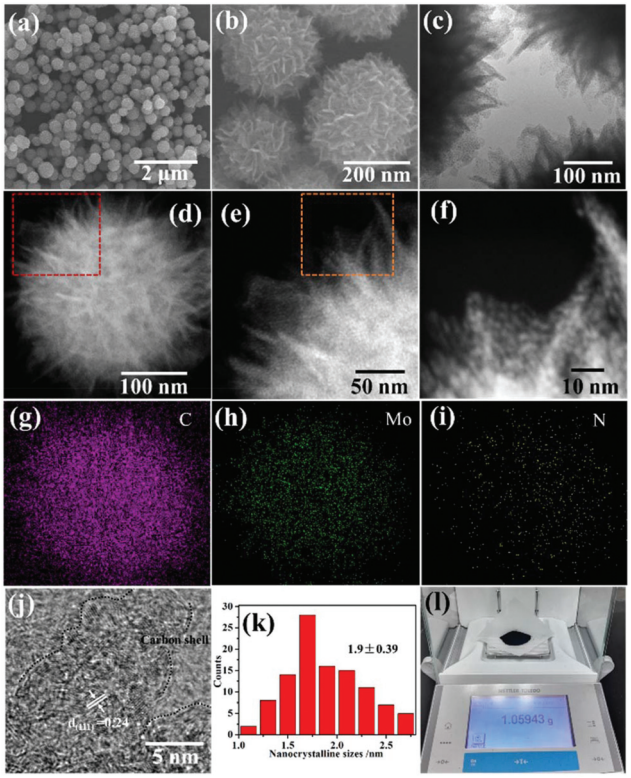

Fig. 2 (a and b) SEM images, (c) TEM image, (d) HAADF-STEM image, (e) local magnified HAADF-STEM image of (d) in a red dashed box, (f) local magnified HAADF-STEM image of (e) in an orange dashed box, (g, h and i) EDX elemental mappings of C, Mo and N elements, respectively, (j) HRTEM image, (k) size distributions of MoC nanocrystallites, and (l) digital photograph of the MoC-HAs product obtained in a large quantity of ≈1.0 g.

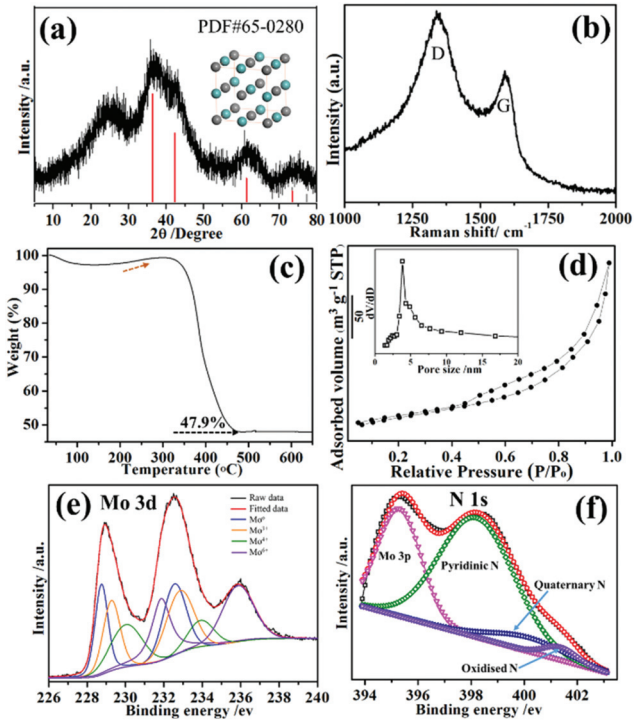

Fig. 3 (a) XRD pattern (inset, crystal view), (b) Raman spectrum, (c) thermogravimetric analysis (TGA), (d) N_2 physisorption isotherm (inset, pore size distribution), XPS Mo 3d (e) and N 1s (f) spectra of electrocatalyst AM-20/WE-54.

whole MoC-HAs with very small sizes. Energy Dispersive X-Ray (EDX, Fig. 2g, h, and i) spectroscopy demonstrates the uniform distribution of C, Mo, and N elements throughout the particles. High-resolution TEM (HRTEM) images indicated that most MoC nanoparticles were typically encapsulated by carbon shells and possess a *d*-spacing of 0.24 nm corresponding to the (111) plane of MoC (Fig. 2j) with a uniform size of generally less than 2 nm (Fig. 2k).[18,23] Previous reports have demonstrated that low-dimension materials (*e.g.* 0D nanoparticles, 1D nanorods and 2D nanosheets) tend to be easily agglomerated with the annealing process in order to decrease the surface energy.[12,13,26] The high dispersion and ultrasmall size of the MoC nanoparticles in MoC-HAs should be ascribed to the *in situ* carbonization of Mo species *via* the confining effect of the carbon sheets, which prohibits the excessive growth and/or further aggregation of MoC nanoparticles. The resultant 3D architectures of MoC-HAs can efficiently prevent the close stacking of 2D carbon nanosheets, which not only improve the structural stability but also provide a large exposed surface for the catalytic purpose. Moreover, as shown in Fig. 2l, the grams of products can be easily obtained, indicating that our proposed synthesis can be highly committed to large-scale production for practical applications.

The XRD pattern of MoC-HAs (Fig. 3a) indicates the presence of characteristic diffraction peaks located at approximately (2θ) 36.9, 42.2, 61.7 and 74.3, which can be ascribed to the MoC structure (PDF#65-0280) (inset).[23] The broad diffraction peaks suggest the very small size of MoC nanocrystallites, indicating that the confined carburization process can be used as an effective protocol for inhibiting further coalescence and crystal growth. The diffraction peak at 2θ = 25.0° should be ascribed to the presence of graphite carbon.[30] The carbon nanosheets are also verified by Raman analysis (Fig. 3b), and the ratios of the G-line (at 1580 cm^{-1}) to D-line (at 1350 cm^{-1}) are used to judge the degree of graphitization. The carbon nanosheets were verified to be amorphous carbon, due to the fact that the G peak is lower than the D peak.[30,31] Fig. 3c shows the thermogravimetric analysis (TGA) curve of AM-20. The initial weight gain in the range of ~150 to 300 °C is due to the gradual oxidation of MoC to MoO_3, and the subsequent significant weight loss should be caused by the combustion of carbon. The weight percentage of MoC in AM-20 was estimated to be about 35.9%, where we assumed that the residues were completely converted to MoO_3 after heating to 650 °C under an oxygen atmosphere. The nitrogen physisorption result of MoC-HAs (Fig. 3d) exhibits an increased nitrogen absorption in the range of relative pressure (P/P_0) from 0.4 to 0.9 due to the capillary condensation phenomenon of nitrogen in the pores of MoC-HAs.[32] MoC-HAs possess a high specific Brunauer–Emmett–Teller surface area (S_{BET}) of 182.2 m^2 g^{-1}.

The pore size distribution curve (Fig. 3d inset) indicates abundant mesopores with a most probable pore size of 3.8 nm. The high specific surfaces areas as well as mesopores of MoC-HAs should be derived from the interconnection of secondary carbon nanosheets and the substantial mass loss of C, H, and O elements during the carburization process.[18] The X-ray photoelectron spectroscopy (XPS) was further used to characterize the valence state and the composition of MoC-HAs. As shown in Fig. 3e, the XPS peak fitting of the Mo 3d suggests the presence of four oxidation states (0, +3, +4, and +6) for Mo species on the surface of MoC-HAs.[23] The Mo^{4+} at 232.9 and 229.7 eV and Mo^{6+} at 235.8 and 231.5 eV should be derived from molybdenum oxides (MoO_2 and MoO_3) that are readily contaminated in air, which are thought to be inactive for the HER. However, Mo^0 (Mo–Mo) and Mo^{3+} (Mo–C) should coexist in molybdenum carbides, serving as the active sites in the HER.[14] The C1s spectrum (Fig. S3†) typically showed three peaks. The main peak at 284.8 eV corresponded to graphite carbon and the C–O and O–C═O bonds at 285.8 eV and 289.4 eV, respectively, were also found in the C1s spectrum.[33] The presence of N in the carbon nanosheets was demonstrated by elemental analysis and XPS results (Fig. 3f). The content of N is tested to be ~1.0 wt% by elemental analysis. Compared with calcination under an Ar atmosphere, an N content of ~0.13 wt% should come from the N_2 activation at 900 °C. The N 1s spectrum of MoC-HAs shows that nitrogen atoms mainly exist in the form of pyridine-N.[33] The result implies that the nitrogen atoms in DA molecules were retained during the carbonization process, resulting in the nitrogen-doped carbon nanosheets. The doped nitrogen is well-known to be beneficial to the conductivity of the carbon nanosheets as well as the interaction of active sites with H^+.[2]

Moreover, the samples in control experiments showed similar XRD patterns (Fig. S4†) and amorphous carbon nanosheet supports (Fig. S5†) with the representative AM-20. The contents of MoC were 36.2% in AM-10, 35.2% in AM-40, 37.1% in WE-18, and 30.3% in WE-81, as determined by thermogravimetric analysis (Fig. S6†). However, we found that as shown in TEM images (Fig. S7†), the samples WE-18 and WE-81 were seriously aggregated after the annealing process. As a result, the two samples showed obviously decreased specific surface areas of 119.9 $m^2\ g^{-1}$ and 76.9 $m^2\ g^{-1}$ of WE-18 and WE-81, respectively, as demonstrated by the nitrogen physisorption results (Fig. S8†). A close observation of WE-81 (Fig. S7b†) implies that small MoC nanoparticles (<5 nm) are still highly dispersed in the fragments. However, the samples AM-10 and AM-40 synthesized with different amounts of $(NH_4)_6Mo_7O_{24}$ show a well-defined 3D spherical assembly and a similar diameter size to AM-20. High specific surface areas of 185.3 $m^2\ g^{-1}$ and 172.8 $m^2\ g^{-1}$ for AM-10 and AM-40, respectively, are obtained (Fig. S9†). The result indicates that the free and oversized carbonaceous nanosheets of WE-18 and WE-81 can be easily aggregated after the annealing process resulting in reduced exposure surfaces for active MoC sites, while the construction of 3D architectures with suitable sizes of the carbonaceous nanosheets can efficiently improve the structural stability of the resultant MoC-HAs.

Based on the aforementioned analyses, MoC-HAs possess unique hierarchical 3D architectures composed of ultrafine MoC nanocrystallites anchored in nitrogen-doped carbon sheets, which show uniform morphologies, high surface areas, and numerous mesopores and thereby are highly desired for the electrocatalysis application.

Electrocatalytic performance of Mo-HAs for the HER

The MoC-HAs are evaluated as an electrocatalyst for the hydrogen evolution reaction (HER) under alkaline conditions. The electrocatalysis was conducted in a H_2-saturated 1 M KOH solution. The electrocatalysts were loaded on a glassy carbon (GC) electrode with the same loading amount of 0.41 mg cm^{-2} and all potentials (overpotentials) were reported *versus* the reversible hydrogen electrode (RHE). The MoC-HAs with varied MoC loadings (AM-10, 20 and 40) and morphologies (aggregated nanosheets of WE-18, hierarchical nanosheet spheres of WE-54, and bulk spheres of WE-81) and Pt/C were studied and the corresponding polarization curves are shown in Fig. 4a. As expected, the commercial Pt/C displayed the highest electrocatalytic activity with an onset overpotential of nearly zero and needed very small overpotentials of 40 mV (η_{10}) and 53 mV (η_{20}) to drive current densities of 10 and 20 mA cm^{-2}. The aggregated nanosheets of the WE-18 (bulk spheres of WE-81) catalyst showed poor HER activity possessing high overpotentials of 220 and 273 mV (255 and 311 mV) at current densities of 10 and 20 mA cm^{-2}, respectively. By contrast, the MoC-HAs with varied MoC loadings exhibited small overpotentials with a rapidly increasing current corresponding to electrochemical hydrogen evolution, implying a high catalytic activity of MoC-HAs towards the HER under alkaline conditions. AM-10 (AM-40) exhibits overpotentials of 166 mV and 206 mV (219 and 241 mV) to drive current densities of 10 and 20 mA cm^{-2}, respectively. In particu-

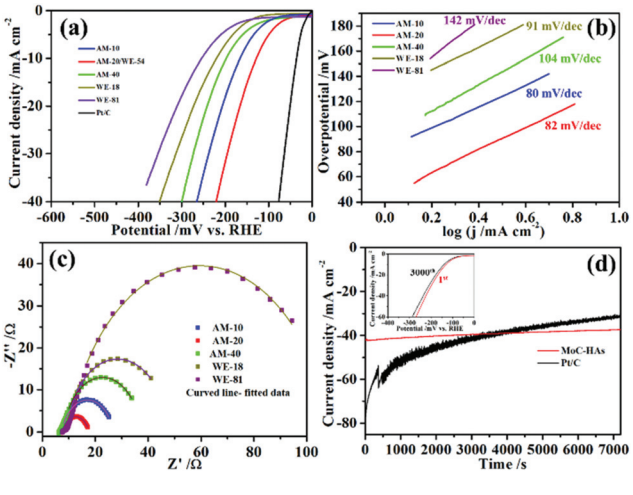

Fig. 4 (a) Polarization curves, (b) Tafel plots, (c) Nyquist plots measured at an overpotential of 180 mV over the frequency range of 100 kHz to 0.01 Hz. (d) The time dependence of current density under a static overpotential of 230 mV over 7200 s for samples MoC-HAs and commercial Pt/C (inset, contrast of polarization curves of the initial and 3000th potential sweeps at 50 mV s^{-1} in 1 M KOH).

lar, AM-20/WE54 possesses the most excellent activity among the prepared electrocatalysts, where very small overpotentials of 128 mV and 170 mV are required to drive current densities of 10 and 20 mA cm^{-2}, respectively. The η_{10} of 128 mV delivered by MoC-HAs (AM-20) is clearly lower than that of the recently reported porous MoC_x nano-octahedra (151 mV),[18] porous carbon-supported Ni/Mo_2C nanorods (197 mV),[12] N–P-doped carbon-supported Ni/Mo_2C (141 mV),[34] porous carbon-supported Mo_2C (165 mV),[19] and MoC@N-doped graphitic carbon nanosheets (220 mV).[35]On comparing with many other representative noble-metal-free electrocatalysts (Table S1†), such as Ni/Mo/Co/W carbides, nitrides, sulfides and phosphides even with various nanostructures,[8,12,17–19,25,34,36–43] MoC-HAs (AM-20) can also be classed as one of the best HER electrocatalysts under alkaline conditions (Table S4†).

Besides, the Tafel plot of AM-20 (Fig. 4b) exhibited a slope of 82 mV dec^{-1}, which is similar to 80 mV dec^{-1} of AM-10 but lower than 104 mV dec^{-1} of AM-40, 91 mV dec^{-1} of WE-18 and 142 mV dec^{-1} of WE-81. Moreover, the electrochemical impedance spectroscopy (EIS) analysis at a selected overpotential of η = 180 mV was performed on these electrocatalysts. As shown in Fig. S10,† EIS Nyquist plots can be well fitted with a two-time-constant model, which consisted of R_s (a series resistance), R_{ct} (at low frequency related to the charge transfer process) and R_p (at high frequency related to the surface porosity).[24] The R_{ct} that is most highly related to the electrochemical performance was compared. As shown in Fig. 4c, the R_{ct} value of AM-20 is 5.2 Ω, which is much smaller than 9.9 Ω of AM-10, 14 Ω of AM-40, 19 Ω of WE-18 and 50 Ω of WE-81 at the same overpotential. The smaller Tafel slope and resistance value of AM-20 should have been resulted from a faster electron transfer, corresponding to its superior HER activity.[3] Based on the aforementioned results, the difference in the HER activities of electrocatalysts can be reasonable. As for WE-18 and WE-81, the lower specific surface areas can be responsible for the poor HER activity. While the cases of AM-10 and AM-40 imply that a suitable composition of active sites (MoC) and conductive supports (carbon nanosheets) can be a meticulous factor for constructing high-performance electrocatalysts. Furthermore, the durability of the electrocatalyst was also important for HER practical applications. To evaluate the stability, the polarization curves after continuous potential sweeps and the time-dependent current density curves tested at a high overpotential of η = 230 mV of the MoC-HAs (AM-20/WE-54) and commercial Pt/C were obtained. As shown in the inset of Fig. 4d,† the activity of MoC-HAs could be maintained with only a small loss of ~15 mV at a current density of 10 mA cm^{-2} after 3000 CV sweeps. As a control, the current density of Pt/C decreased dramatically (Fig. 4d) leading to poor stability. However, the time-dependent current density curve of MoC-HAs (Fig. 4d) demonstrates a minor current drop at the beginning and a stabilized current density of about 95% of the initial value after ~1000 s. The above stability tests indicate the high stability of AM-20 for the HER.

Taken together, we suggest that the high electrocatalytic HER performance of MoC-HAs can be ascribed to the following merits: (1) ultra-small MoC nanocrystallites (~2 nm) formed *via in situ* carbonization provide an enhanced exposure of surface active sites. (2) The nitrogen-doped carbon nanosheets can enhance the electronic conductivity, facilitating the charge transfer between the active sites during the HER process. (3) High specific surface areas (182.2 m^2 g^{-1}) and numerous mesopores (3.8 nm) of MoC-HAs can facilitate the contact between the electrolyte and electrocatalyst and ensure efficient utilization of the active sites, promoting the charge and mass transfer during the HER. (4) The unique 3D architectures composed of MoC nanoparticles confined by carbon sheets can efficiently prevent the excessive growth of ultrafine MoC and the aggregation of carbon nanosheets and thus provide good stability during long-term operation.

Conclusion

In summary, we have constructed a hierarchical 3D self-assembly electrocatalyst composed of ultrafine MoC nanoparticles encapsulated by nitrogen-doped carbon nanosheets for efficient hydrogen production. Ultrafine active sites can be well restricted by the *in situ* confinement carbonization of Mo species within the conducting carbon nanosheets. The resultant hierarchical 3D architectures exhibit remarkable electrocatalytic performance and structural stability for HER tests, which should be ascribed to the highly exposed active sites and facilitated electron/ion transport pathways resulting from the merits of the composition and configuration or the cooperative/synergistic effects of ultrafine MoC nanoparticles, N-doped carbon nanosheet conductive supports, high specific surface areas and mesoporous structures. We expect that our findings offer new perspectives in materials chemistry and open up exciting opportunities for preparing high-performance non-noble-metal catalysts, such as metal carbides, nitrides and phosphides for electrocatalytic applications.

Conflicts of interest

There are no conflicts to declare.

Acknowledgements

This work was supported by the NSFC (21431003, 21521091), China Ministry of Science and Technology under Contract of 2016YFA0202801 and the China Postdoctoral Science Foundation (No. 043260382).

References

1 M. S. Dresselhaus and I. L. Thomas, *Nature*, 2001, **414**, 332.
2 Y. Liu, G. Yu, G. D. Li, Y. Sun, T. Asefa, W. Chen and X. Zou, *Angew. Chem., Int. Ed.*, 2015, **54**, 10752.

3 W. F. Chen, C. H. Wang, K. Sasaki, N. Marinkovic, W. Xu, J. T. Muckerman, Y. Zhu and R. R. Adzic, *Energy Environ. Sci.*, 2013, **6**, 943.
4 H. Wang, H. Lin, Y. Long, B. Ni, T. He, S. Zhang, H. Zhu and X. Wang, *Nanoscale*, 2017, **9**, 2074.
5 H. Ang, H. T. Tan, Z. M. Luo, Y. Zhang, Y. Y. Guo, G. Guo, H. Zhang and Q. Yan, *Small*, 2015, **11**, 6278.
6 J.-S. Li, Y. Wang, C.-H. Liu, S.-L. Li, Y.-G. Wang, L.-Z. Dong, Z.-H. Dai, Y.-F. Li and Y.-Q. Lan, *Nat. Commun.*, 2016, **7**, 11204.
7 Z. Xing, Q. Liu, A. M. Asiri and X. Sun, *ACS Catal.*, 2015, **5**, 145.
8 M. Gong, W. Zhou, M. C. Tsai, J. G. Zhou, M. Y. Guan, M. C. Lin, B. Zhang, Y. F. Hu, D. Y. Wang, J. Yang, S. J. Pennycook, B. J. Hwang and H. J. Dai, *Nat. Commun.*, 2014, **5**, 6.
9 S. Wang, X. Gao, X. Hang, X. Zhu, H. Han, W. Liao and W. Chen, *J. Am. Chem. Soc.*, 2016, **138**, 16236.
10 S. Wang, J. Wang, M. Zhu, X. Bao, B. Xiao, D. Su, H. Li and Y. Wang, *J. Am. Chem. Soc.*, 2015, **137**, 15753.
11 H. Vrubel and X. Hu, *Angew. Chem., Int. Ed.*, 2012, **51**, 12703.
12 Z.-Y. Yu, Y. Duan, M.-R. Gao, C.-C. Lang, Y.-R. Zheng and S.-H. Yu, *Chem. Sci.*, 2017, **8**, 968.
13 Y. Mu, Y. Zhang, L. Fang, L. Liu, H. Zhang and Y. Wang, *Electrochim. Acta*, 2016, **215**, 357.
14 R. Ma, Y. Zhou, Y. Chen, P. Li, Q. Liu and J. Wang, *Angew. Chem., Int. Ed.*, 2015, **54**, 14723.
15 J. Duan, S. Chen, B. A. Chambers, G. G. Andersson and S. Z. Qiao, *Adv. Mater.*, 2015, **27**, 4234.
16 X. Yu, S. Zhang, C. Li, C. Zhu, Y. Chen, P. Gao, L. Qi and X. Zhang, *Nanoscale*, 2016, **8**, 10902.
17 X. X. Zou, X. X. Huang, A. Goswami, R. Silva, B. R. Sathe, E. Mikmekova and T. Asefa, *Angew. Chem., Int. Ed.*, 2014, **53**, 4372.
18 H. B. Wu, B. Y. Xia, L. Yu, X.-Y. Yu and X. W. Lou, *Nat. Commun.*, 2015, **6**, 6512.
19 M. Qamar, A. Adam, B. Merzougui, A. Helal, O. Abdulhamid and M. N. Siddiqui, *J. Mater. Chem. A*, 2016, **4**, 16225.
20 C. Tan, X. Cao, X.-J. Wu, Q. He, J. Yang, X. Zhang, J. Chen, W. Zhao, S. Han, G.-H. Nam, M. Sindoro and H. Zhang, *Chem. Rev.*, 2017, **117**, 6225.
21 Y. Zheng, Y. Jiao, L. Ge, M. Jaroniec and S. Z. Qiao, *Angew. Chem., Int. Ed.*, 2013, **52**, 3110.
22 Y. Zhao, K. Kamiya, K. Hashimoto and S. Nakanishi, *J. Am. Chem. Soc.*, 2015, **137**, 110.
23 C. Wan, Y. N. Regmi and B. M. Leonard, *Angew. Chem., Int. Ed.*, 2014, **53**, 6407.
24 X. Xu, F. Nosheen and X. Wang, *Chem. Mater.*, 2016, **28**, 6313.
25 H. Vrubel and X. L. Hu, *Angew. Chem., Int. Ed.*, 2012, **51**, 12703.
26 P. P. Wang, H. Y. Sun, Y. J. Ji, W. H. Li and X. Wang, *Adv. Mater.*, 2014, **26**, 964.
27 W. Cui, N. Cheng, Q. Liu, C. Ge, A. M. Asiri and X. Sun, *ACS Catal.*, 2014, **4**, 2658.
28 Z. Zhang, Y. Chen, S. He, J. Zhang, X. Xu, Y. Yang, F. Nosheen, F. Saleem, W. He and X. Wang, *Angew. Chem., Int. Ed.*, 2014, **53**, 12517.
29 X. Li, X. Niu, W. Zhang, Y. He, J. Pan, Y. Yan and F. Qiu, *ChemSusChem*, 2017, **10**, 976.
30 C. Tang, Z. Wu and D. Wang, *ChemCatChem*, 2016, **8**, 1961.
31 C. Du, H. Huang, Y. Wu, S. Wu and W. Song, *Nanoscale*, 2016, **8**, 16251.
32 H. Wang, W. Qian, S. Gao, J. Du, J. Chen, Y. Kong and J. Wang, *Appl. Catal., A*, 2015, **504**, 228.
33 J. Yang, F. Zhang, X. Wang, D. He, G. Wu, Q. Yang, X. Hong, Y. Wu and Y. Li, *Angew. Chem., Int. Ed.*, 2016, **55**, 12854.
34 L. Ji, J. Wang, L. Guo and Z. Chen, *J. Mater. Chem. A*, 2017, **5**, 5178.
35 J. Zhu, K. Sakaushi, G. Clavel, M. Shalom, M. Antonietti and T.-P. Fellinger, *J. Am. Chem. Soc.*, 2015, **137**, 5480.
36 J. X. Zhu, K. Sakaushi, G. Clavel, M. Shalom, M. Antonietti and T. P. Fellinger, *J. Am. Chem. Soc.*, 2015, **137**, 5480.
37 P. Xiao, Y. Yan, X. M. Ge, Z. L. Liu, J. Y. Wang and X. Wang, *Appl. Catal., B*, 2014, **154**, 232.
38 X. J. Fan, H. Q. Zhou and X. Guo, *ACS Nano*, 2015, **9**, 5125.
39 J. L. Shi and J. M. Hu, *Electrochim. Acta*, 2015, **168**, 256.
40 M. Gong, W. Zhou, M. J. Kenney, R. Kapusta, S. Cowley, Y. P. Wu, B. A. Lu, M. C. Lin, D. Y. Wang, J. Yang, B. J. Hwang and H. J. Dai, *Angew. Chem., Int. Ed.*, 2015, **54**, 11989.
41 L. L. Feng, G. T. Yu, Y. Y. Wu, G. D. Li, H. Li, Y. H. Sun, T. Asefa, W. Chen and X. X. Zou, *J. Am. Chem. Soc.*, 2015, **137**, 14023.
42 P. Xiao, M. A. Sk, L. Thia, X. M. Ge, R. J. Lim, J. Y. Wang, K. H. Lim and X. Wang, *Energy Environ. Sci.*, 2014, **7**, 2624.
43 J. Q. Tian, Q. Liu, A. M. Asiri and X. P. Sun, *J. Am. Chem. Soc.*, 2014, **136**, 7587.